RARE METALS

ORIGINAL ARTICLE

A Hf-doped dual-phase high-entropy alloy: phase evolution and wear features

Hao Ren, Rui-Run Chen* , Xue-Feng Gao, Tong Liu, Gang Qin, Yu-Lung Chiu, Shi-Ping Wu, Jing-Jie Guo

Abstract Initially defined high entropy alloys (HEAs) usually exhibit a single-phase solid-solution structure. However, two and/or more types of phases in HEAs possibly induce the desired microstructure features, which contribute to improving the wear properties of HEAs. Here, we prepare a series of $(AlCoCrFeNi)_{100-x}Hf_x$ ($x = 0, 2, 4$ and 6; at%) HEAs and concern their phase compositions, microstructures and wear properties. Hf leads to the formation of $(Ni, Co)_2Hf$-type Laves phase and tailors the microstructure from a body-centered cubic (BCC) single-phase structure to a hypoeutectic structure. An increased hardness from $\sim$ HV 512.3 to $\sim$ HV 734.1 is due to solid-solution strengthening, grain refinement strengthening and precipitated phase strengthening. And a few oxides $(Al_2O_3 + Cr_2O_3)$ caused by the wear heating contribute to an 85.5% decrease in wear rate of the HEA system from 6.71×10^{-5} to 0.97×10^{-5} $m^3 \cdot N^{-1} \cdot m^{-1}$. In addition, Hf addition changes the wear mechanism from abrasive wear, mild oxidative wear and adhesive wear to oxidative wear and adhesive wear.

Keywords High entropy alloy; Laves phase; Hardness; Wear mechanism

H. Ren, R.-R. Chen*, X.-F. Gao, T. Liu, G. Qin, S.-P. Wu, J.-J. Guo
National Key Laboratory for Precision Hot Processing of Metals, School of Materials Science and Engineering, Harbin Institute of Technology, Harbin 150001, China
e-mail: ruirunchen@hit.edu.cn

Y.-L. Chiu
School of Metallurgy and Materials, University of Birmingham, Edgbaston, Birmingham B15 2TT, UK

1 Introduction

High entropy alloys (HEAs), which are regarded as one kind of innovative materials, have received a lot of attention [1–5]. In general, HEAs consist of multiple elements and are in a single-phase solid solution [6–8]. The solid-solution structure can not only contribute to the solid-solution hardening caused by the multi-element interactions but also modify the ductility due to lacking interphase boundaries [9]. Consequently, HEAs show many desired properties, namely, high strength and hardness, suitable ductility, and excellent thermal stability, etc. [8, 10–20]. For example, AlCoCrFeNi HEA possesses a Vickers hardness higher than HV 520 and a compressive yield strength between 1138 and 1702 MPa [11]. Based on the Archard rule under dry wear conditions [21], there is an inversely proportional relationship between wear rate and material hardness (or strength). Therefore, HEAs are expected to exhibit excellent anti-wear properties [22–30].

Investigations on wear-resistant HEA materials manifest that the improved wear properties of these HEAs are mainly associated with multiple phases in materials, and precipitated phase strengthening plays an essential role in different strengthening mechanisms [31–36]. For instance, Chuang et al. [31] assessed the effects of Al and Ti contents on phases, microstructures, and wear properties of $Al_xCo_{1.5}CrFeNi_{1.5}Ti_y$ HEAs. Al and Ti could tailor the phase compositions of the HEAs, particularly in the volume fraction of hard η phase, thus improving their wear resistance. Furthermore, the formation of a boride phase [37] or TiC [38] ceramic–metal composite enhances the HEA hardness, thus, the wear resistance.

Because of good overall performance of AlCoCrFeNi containing A2 and B2 phases, it catches numerous attention [39–43]. Many metallic elements, i.e., Nb [44] and Zr [45],

are added into AlCoCrFeNi HEA to produce the hard precipitated phase to modify the mechanical performance. The atomic radius of Hf is almost the same as that of Zr but larger than that of Nb [46]. Meanwhile, the mixing enthalpies between Hf and other constituent elements in AlCoCrFeNi HEA are a little more positive than those between Zr and constituent elements and more negative than those between Nb and constituent elements [47]. What occurs when add Hf into AlCoCrFeNi HEA?

In this work, we design a group of $(AlCoCrFrNi)_{100-x}Hf_x$ ($x = 0, 2, 4$ and 6; at%) HEAs. The effect of Hf addition on phases and microstructures of the HEAs is revealed. And the wear properties of $(AlCoCrFrNi)_{100-x}Hf_x$ HEAs are studied. This work opens other doors on the potential microstructure features that cause the superior wear-resistant properties of AlCoCrFeNi HEA.

2 Experimental

The pure Al, Co, Cr, Fe, Ni and Hf particles with the purity higher than 99.9% (DM Material Inc., Beijing, China) were received as raw materials and compounded through arc melting in an argon atmosphere. For getting the uniform composition, each ingot ($\Phi45$ mm $\times$ 10 mm) was re-melted at least six times. The crystal structures of HEAs were determined by X-ray diffraction (XRD, Empyrean, Netherland) with Cu Kα radiation scanning from 20° to 100° at a rate of 4 (°)·min^{-1}. The microstructure morphology of each HEA ingot was observed using scanning electron microscopy (SEM, Merlin Compact, Zeiss, Germany) operated at 20 kV. Transmission electron microscopy (TEM) and EDS high-angle annular dark-field (EDS-HAADF) analyses were carried out by using an FEI-Talos F200X microscope operated at 200 kV.

The Vickers hardness (HV-1000, Shanghai Lianer Testing Equipment Co., China) was recorded at a load of 300 g for 10 s. For dry wear tests, the specimens with dimensions of $\Phi25$ mm $\times$ 3 mm were fabricated by wire cutting from the as-cast ingots. Prior to the wear test, all specimens were firstly ground against 400-, 800-, 1200- and 2000-grit sandpaper and then mechanically polished with diamond paste (W1.5). The surface roughness (R_a) values determined by atomic force microscopy (AFM, Dimension Fastscan, Bruker, Germany) for Hf-0, Hf-2, Hf-4 and Hf-6 HEAs are around 4.34, 2.59, 4.62 and 5.10 nm, respectively. The dry wear test parameters (MS-T3000, Lanzhou Huafeng Technology Co., Ltd. China) were load of 5 N, sliding speed of 300 r·min^{-1}, track radius of 6 mm, sliding time of 30 min and Si$_3$N$_4$ ball ($\Phi6$ mm), at room temperature. The three-dimensional morphologies and profiles of $(AlCoCrFrNi)_{100-x}Hf_x$ HEAs after dry wear tests were obtained by

white light interferometer (Contour GT-X3, Bruker, Tucson, AZ, USA).

3 Results and discussion

3.1 Phase composition and microstructures

Figure 1a presents XRD patterns of $(AlCoCrFrNi)_{100-x}Hf_x$ HEAs. A2 and B2 body-centered cubic (BCC) phases are found in each HEA. And some new diffraction peaks originating from (Ni, Co)$_2$Hf-type Laves phase appear in three Hf-doped HEAs. By adding Hf, the peak intensity of Laves phase increases, manifesting that the volume fraction of Laves phase increases. Besides, the $(110)_{BCC}$ diffraction peak shifts towards a lower reflection angle, as learnt from Fig. 1b. This suggests that the dissolution of Hf atom in BCC phase can induce a more serious lattice distortion compared with Hf-0 HEA.

For SEM observation of Hf-0 HEA, Fig. 1c illustrates the single-phase morphology. When Hf is introduced (Fig. 1d–f), i.e., Hf-2, -4 and -6 HEAs, the hypoeutectic structure composed of BCC phase and eutectic phase is obtained. The eutectic phase is composed of alternating BCC phase and Laves phase. More Hf addition causes a higher volume fraction of Laves phase, according well with XRD results.

Figure 1g shows the chemical distribution maps of Hf-6 HEA. In the primary BCC phase, the dendrite core (DR) region has (Ni, Al)-rich composition, whereas the inter-dendrite (ID) region displays (Fe, Cr)-rich composition. In Laves phase region, Ni, Co and Hf segregate. Table 1 shows the chemical compositions of various regions in Hf-6 HEA. The primary BCC phase (Zone 1) is enriched with Fe, Cr and Al but depleted of Ni, Co and Hf, which is opposite to the Laves phase (Point 3). In general, the chemical composition of each element in Zone 2 is almost half of the sum of these in Zone 1 and Point 3. This proves that the eutectic phase consists of the BCC phase and Laves phase. The higher contents of Ni, Co and Hf in Laves phase are due to the negative mixing enthalpies (Table 2 [46, 47]) and large electronegativity (Table 3 [48]) of Ni–Hf and Co–Hf atomic pairs.

Figures 2, 3 show TEM morphologies, SAED patterns and chemical composition maps of Hf-0 and Hf-2 HEAs. As learnt from Fig. 2a, b, d, e, the cubic or rod-like A2 precipitates (disordered phase) and continuous B2 matrix (ordered phase) are found. A difference in nm-sized morphologies of DR and ID regions is ascribed to the type of order of the domains and strain [49]. Figure 2c, f reveals the elemental distribution maps of Hf-0 HEA. The A2 phase is enriched with Fe and Cr but depleted of Ni and Al, which is opposite to the B2 phase. The Co is uniformly
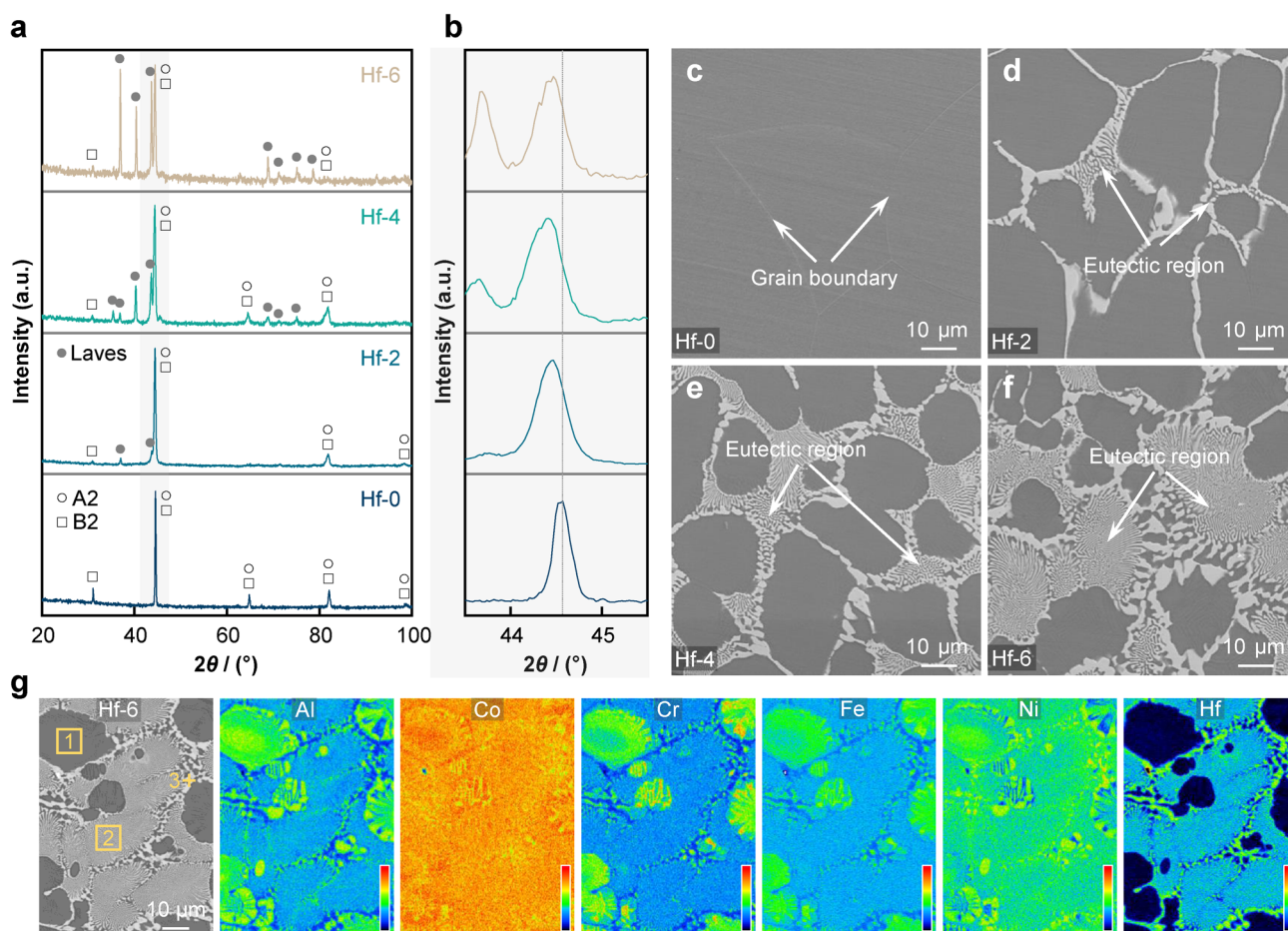
Fig. 1 a, b XRD patterns and **c–f** SEM images of HEAs as well as **g** elemental distribution maps of Hf-6 HEA

Table 1 Chemical distribution of various regions in Hf-6 HEA (at%)

Zone	Al	Co	Cr	Fe	Ni	Hf
Nominal	18.80	18.80	18.80	18.80	18.80	6.00
BCC primary phase (Zone 1)	22.10	17.99	21.05	19.12	18.49	1.25
Eutectic region (Zone 2)	13.97	20.43	16.80	17.82	19.64	11.35
Laves-rich region (Point 3)	7.67	22.18	9.78	16.39	22.45	21.53

Table 2 Mixing enthalpy (kJ·mol^{-1}) between two components and atomic radius (nm)

Element (atom radius)	Al	Co	Cr	Fe	Ni	Hf
Al (0.143)	0	− 19	− 10	− 11	− 22	− 39
Co (0.125)		0	− 4	− 1	0	− 35
Cr (0.128)			0	− 1	− 7	− 9
Fe (0.126)				0	− 2	− 21
Ni (0.124)					0	− 42
Hf (0.159)						0

Table 3 Electronegativity of various constituent elements in Al–Co–Cr–Fe–Ni–Hf HEA system

Element	Al	Co	Cr	Fe	Ni	Hf
Electronegativity	1.61	1.88	1.66	1.83	1.91	1.30

distributed. Figure 3a–c shows TEM images of Hf-2 HEA. In the eutectic region, the alternately grown BCC and Laves phases are further testified by SAEDs (Fig. 3d$_1$–d$_3$).
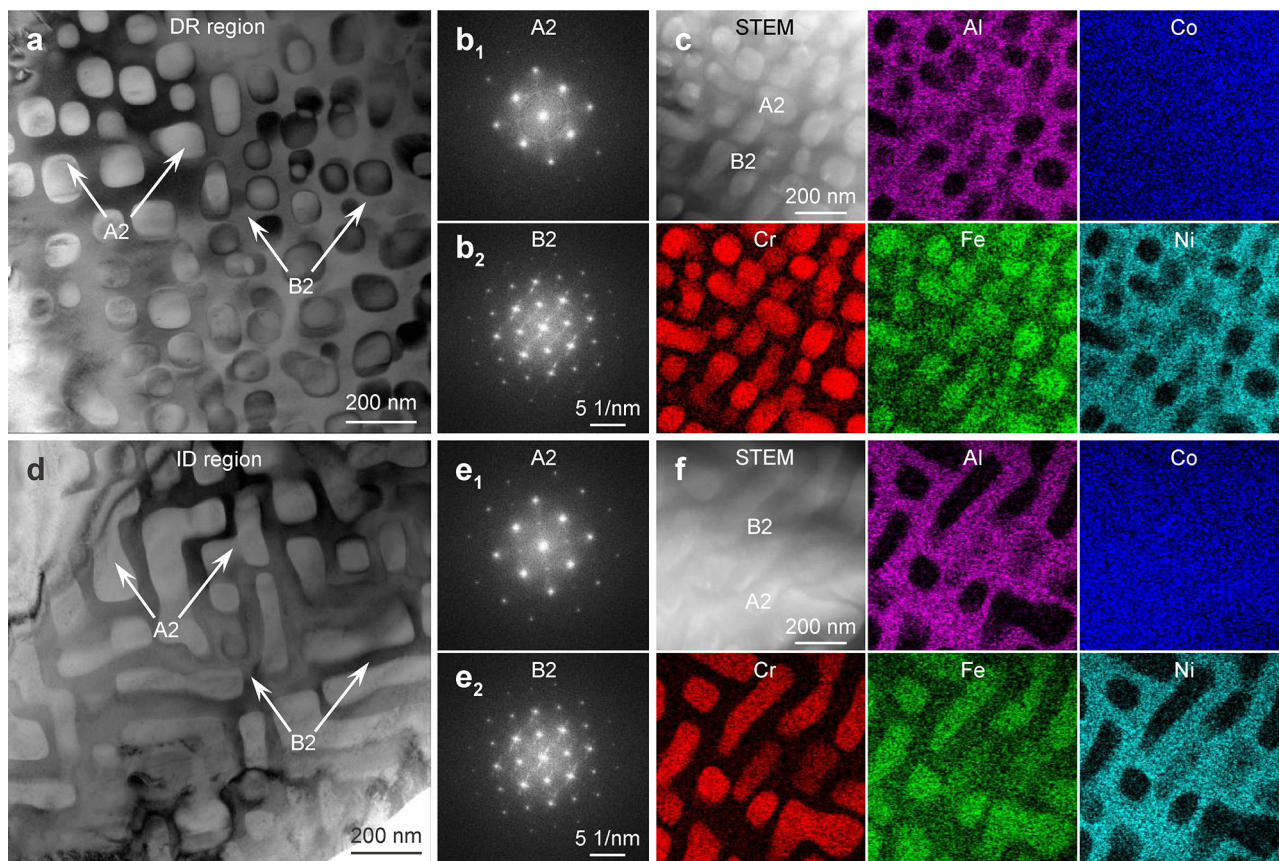
Fig. 2 **a–d** TEM images, **b₁, b₂, e₁, e₂** SAED patterns, and **c, f** elemental composition maps of Hf-0 HEA

And the numerous stacking faults and twins are discovered in Laves phase of an as-casted HEA, which is in accordance with Refs. [50–52]. As seen in Fig. 3e, f, Laves phase is (Hf, Ni and Co)-rich, agreeing well with EMPA results (Fig. 1g).

3.2 Mechanical properties

The Vickers hardness values of $(AlCoCrFrNi)_{100−x}Hf_x$ HEAs are collected in Fig. 4a. By increasing Hf addition, the Vickers hardness enhances from $\sim$ HV 512.3 to $\sim$ HV 734.1. The hardness enhancement is resulted from three strengthening mechanisms: solid-solution strengthening, fine-grain strengthening, and precipitated phase strengthening. As learnt from Fig. 1b, the dissolution of Hf atoms in BCC phase can cause a more serious lattice distortion relative to Hf-0 HEA. Among the four HEAs, the most serious lattice distortion takes place in Hf-6 HEA. However, the dissolution content of Hf atoms in Hf-6 HEA is only 1.25 at% (Table 1), which is too lower to be responsible for the total Vickers hardness increments of $(AlCoCrFrNi)_{100−x}Hf_x$ HEAs.

Meanwhile, fine-grain strengthening has also made some contributions due to the "Hall–Petch" relationship [53, 54] as follows:

$$\sigma_y = \sigma_0 + \frac{k_y}{d^{1/2}} \tag{1}$$

where σ_y is the yield stress, σ_0 stands for the lattice friction stress, k_y (182 MPa·μm$^{1/2}$ [55]) denotes the strengthening coefficient and d is the mean grain diameter. According to Eq. (1), an increase in yield strength ascribed to the grain size difference ($\Delta\sigma_G$) is described as:

$$\Delta\sigma_G = k_y \left(d_H^{-1/2} - d_0^{-1/2} \right) \tag{2}$$

where d_H denotes the grain size of the Hf-doped HEA (Hf-2, Hf-4 and Hf-6 HEAs), and d_0 is the grain size of Hf-0 HEA. Based on Fig. 1c–f, the mean grain sizes of Hf-0, Hf-2, Hf-4 and Hf-6 HEAs are $d_0 = 141.6$ μm, $d_{Hf-2} = 61.7$ μm, $d_{Hf-4} = 45.9$ μm, and $d_{Hf-6} = 31.1$ μm, respectively. The strength contribution values of fine-grain strengthening on Hf-2, Hf-4 and Hf-6 HEAs are 7.88, 11.58, and 17.35 MPa, respectively. It should be noted that the strength of an alloy follows a linear relationship with the hardness of an alloy, which fits with Tabor's findings [56], i.e.,

$$H = c \times \sigma_y \tag{3}$$

where c (3.3) is the proportionality factor based on Ref. [57]. Therefore, the calculated hardness increments corresponding
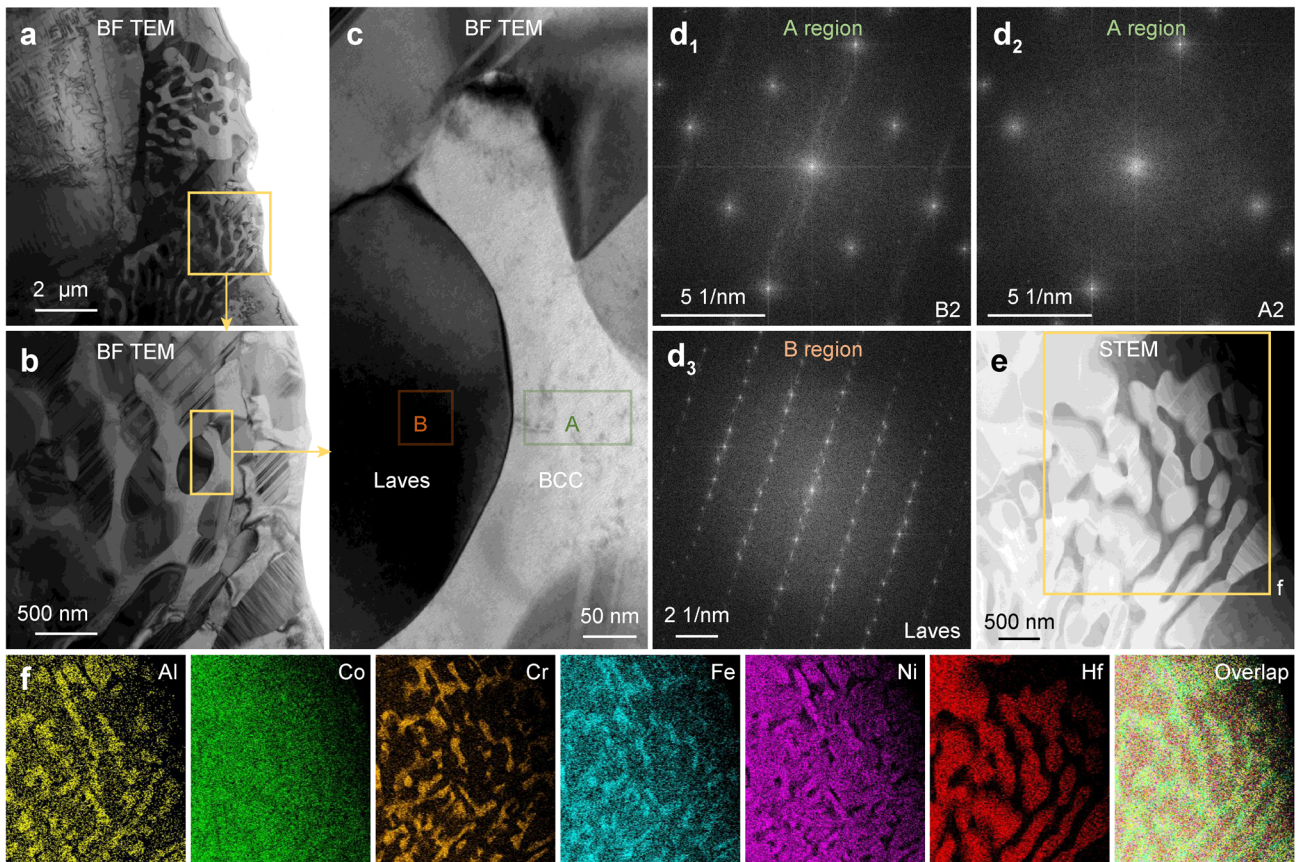
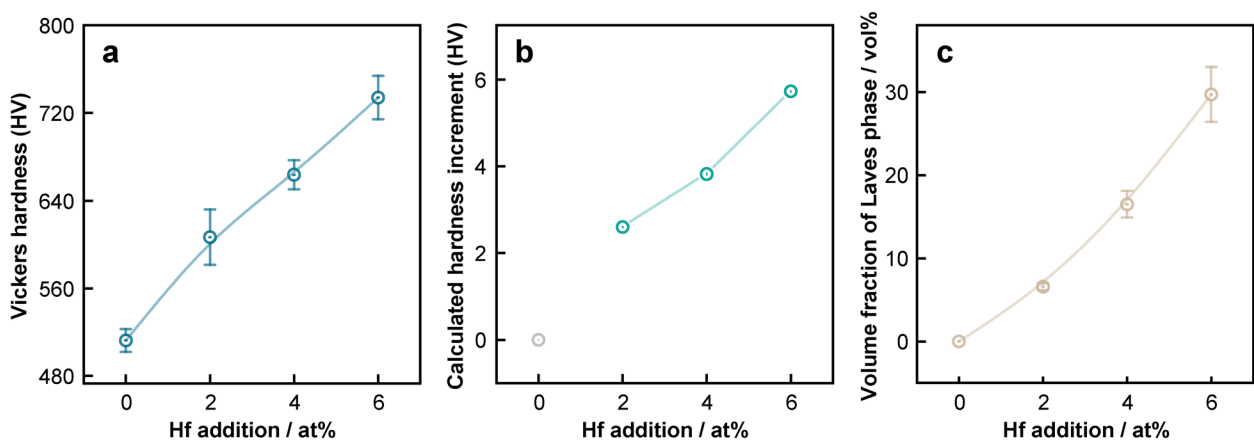**Fig. 3 a–c, e** TEM images, **d₁–d₃** SAED patterns, and **f** elemental composition maps of Hf-2 HEA

Fig. 4 a Vickers hardness, **b** calculated hardness increase and **c** volume fraction of Laves phase of $(AlCoCrFrNi)_{100-x}Hf_x$ HEAs

to the fine-grain strengthening for Hf-2, Hf-4, and Hf-6 HEAs are ~ HV 2.60, ~ HV 3.82, and ~ HV 5.73, respectively (Fig. 4b). The calculated hardness increments are too small to account for the total hardness increase.

Figure 4c elucidates the relationship between the volume fraction of Laves phase and Hf addition. By adding Hf from 0 to 6 at%, the volume fraction of Laves phase increases from 0 to 29.7 vol%. In consequence, the Vickers hardness is enhanced from HV 512.3 to HV 734.1. This

indicates that precipitated phase strengthening acts as a vital role in the total Vickers hardness increase of $(AlCoCrFrNi)_{100-x}Hf_x$ HEAs.

3.3 Wear features

The coefficient of friction (COF), regarded as a basic parameter of a friction system, is related to the resistance between an alloy and a friction pair. When the test is

conducted under the same conditions, the microstructure and surface roughness play a vital role on the COF. The COF curves of $(AlCoCrFrNi)_{100-x}Hf_x$ HEAs are depicted in Fig. 5a. Some severe fluctuations during the running-in process are caused by the ragged grinding between HEA and friction pair. After this running-in process of appropriately 10 min, there are four relatively stable COF curves. During the relatively stable process, both instrument vibration and measurement accuracy lead to the fluctuation of COF value [58]. To accurately compare COF values of $(AlCoCrFrNi)_{100-x}Hf_x$ HEAs, Fig. 5b shows the average COF values collected from the relatively stable period of COF curves. The COF values of Hf-0, -2, -4 and -6 HEAs are 0.53, 0.46, 0.35 and 0.28, respectively. By adding Hf, the COF value decreases. Tailoring the alloy microstructure results in the increase of Vickers hardness and thereby reduces the COF value [10, 58], agreeing well with this work.

The 3D worn morphologies of $(AlCoCrFrNi)_{100-x}Hf_x$ HEAs are shown in Fig. 6. When Hf addition increases from 0 to 6 at%, the distance and depth of wear track of Hf-doped HEAs gradually decrease, indicating the anti-wear property improvement of Hf-doped HEAs. Figure 7 displays the wear rates of $(AlCoCrFrNi)_{100-x}Hf_x$ HEAs. With increasing Hf element, the Vickers hardness increases (Fig. 4a), and the wear rate decreases from 6.71×10^{-5} to 0.97×10^{-5} m$^3 \cdot$N$^{-1} \cdot$m^{-1}, agreeing well with Archard's rule [21].

Figure 8 shows the worn morphologies of $(AlCoCrFrNi)_{100-x}Hf_x$ HEAs. On the wear track surface of Hf-0 HEA, the wear debris island and scattered wear debris are detected. The formation of the wear debris island is caused by the accumulation and compaction of wear debris [59].
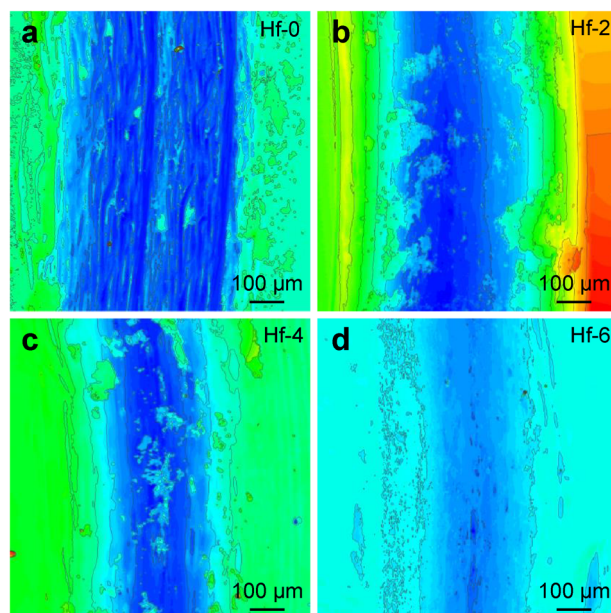

Fig. 6 3D worn morphologies of $(AlCoCrFeNi)_{100-x}Hf_x$ HEAs

Si and O are found on the surface of wear debris island. Meanwhile, O is obtained on the wear track surface of Hf-0 HEA (Table 4). Hence, the wear mechanism of Hf-0 HEA is affirmed to be abrasive wear, adhesive wear, and mild oxidative wear. For Hf-2, -4 and -6 HEAs, many wear grooves and wear debris are present on their wear track surfaces instead of the wear debris island. It is noted that O content on the wear track surfaces increases by adding Hf, manifesting that oxidative wear plays an increasingly crucial role. As a result, the wear mechanisms of Hf-2, -4 and -6 HEAs are oxidative wear and adhesive wear.
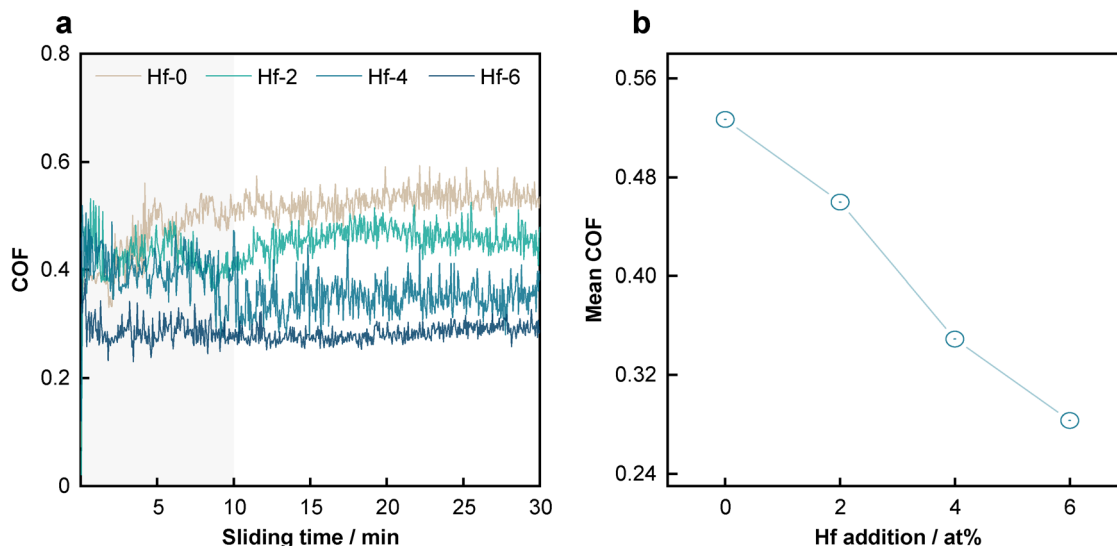

Fig. 5 a Coefficient of friction (COF) curves and **b** mean COF values of $(AlCoCrFeNi)_{100-x}Hf_x$ HEAs
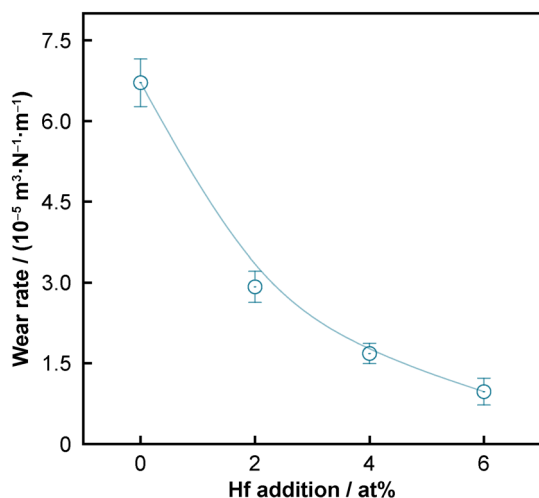
Fig. 7 Wear rate values of $(AlCoCrFeNi)_{100-x}Hf_x$ HEAs

In Table 4, the chemical compositions of wear track surfaces of $(AlCoCrFrNi)_{100-x}Hf_x$ HEAs are testified by EDS. An increasing O content suggests that more oxides are produced on the wear track surfaces of Hf-doped HEAs. In order to identify the phase compositions of oxides on worn surfaces, Raman spectra of four $(AlCoCrFrNi)_{100-x}Hf_x$ HEAs are carried out and displayed in Fig. 9a. On the outside of wear track surface, no oxides are observed. For Hf-0 HEA, there is only a small number of Al_2O_3 and Cr_2O_3 oxides on the inside of the worn surface. The Vickers hardness of Hf-doped HEAs is higher than that of Hf-0 HEA. Therefore, Hf-doped HEAs are strong enough to resist the wear against the Si_3N_4 ball, and the alloy surface will not be worn off quickly during the wear test. Indeed, they can withstand being worn for a long time and are thus continuously heated due to friction. Such frictional heating raises the temperature of the local contact areas on the surface, causing serious surface oxidation [31, 38]. As a result, for Hf-6 HEA, there are a large number of Al_2O_3 and Cr_2O_3 oxides. Al_2O_3 and Cr_2O_3 oxides protect the Hf-doped HEAs from direct contact with friction pair and reduce the degree of adhesive wear [60, 61]. Thus, the wear rate of the Hf-doped HEAs is further decreased. The reason why Al_2O_3 and Cr_2O_3 oxides form rather than other oxides is correlated with the lowest Gibbs free energy of the formation of Al_2O_3 and Cr_2O_3 oxides, as shown in Fig. 9b.

4 Conclusion

To summarize, the phase compositions, microstructure features and wear properties of $(AlCoCrFrNi)_{100-x}Hf_x$

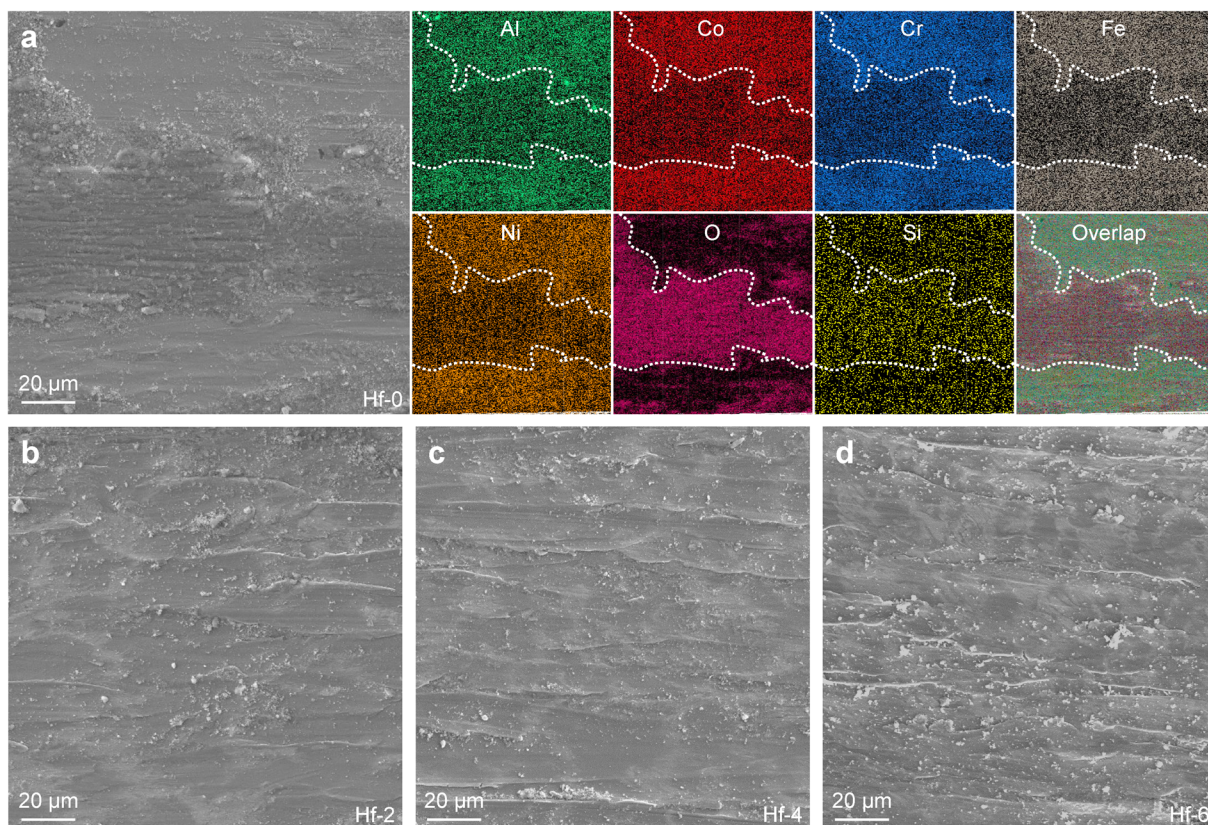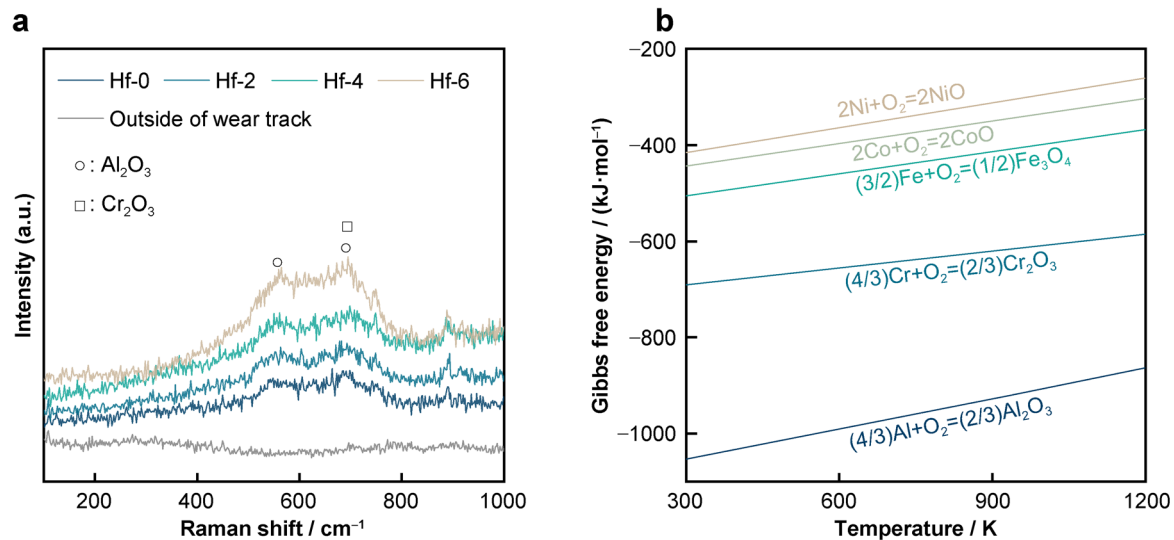Fig. 8 SEM images of worn morphologies of $(AlCoCrFeNi)_{100-x}Hf_x$ HEAs: a Hf-0; b Hf-2; c Hf-4; d Hf-6

Table 4 Compositions (at%) of wear track surfaces in $(AlCoCrFeNi)_{100-x}Hf_x$ HEAs by EDS

HEA	Al	Co	Cr	Fe	Ni	Hf	O	Si
Hf-0	20.50	19.22	20.33	19.26	18.02	–	2.42	0.24
Hf-2	22.63	16.57	16.36	16.26	17.37	1.36	9.12	0.33
Hf-4	18.47	15.36	15.30	15.24	15.40	2.13	17.98	0.12
Hf-6	15.65	14.69	13.75	13.77	13.95	4.06	24.06	0.06

Fig. 9 **a** Raman spectra of $(AlCoCrFeNi)_{100-x}Hf_x$ HEAs and **b** Ellingham diagram of Al_2O_3, Cr_2O_3, Fe_3O_4, CoO and NiO oxides [62]

HEAs are studied. Hf addition changes the original phase constitution, which yields the formation of $(Ni, Co)_2Hf$-type Laves phase besides the original solid solution phase. This causes the microstructure evolution from a BCC solid solution to a hypoeutectic structure. By increasing the Hf addition, the Vickers hardness enhances from HV 512.3 to HV 734.1, which is related to solid-solution strengthening, fine-grain strengthening and precipitated phase strengthening. The elevated hardness of Hf-doped HEAs and the formed oxides (Al_2O_3 + Cr_2O_3) resulting from the wear heating contribute to a downward wear rate, thus changing the wear mechanism from abrasive wear, adhesive wear and mild oxidative wear to oxidative wear and adhesive wear. The high-performance AlCoCrFeNiHf HEAs have broad application prospects in the mechanical equipment which are used in extreme conditions in the future.

Declarations

References

[1] Ye YX, Liu CZ, Wang H, Nieh TG. Friction and wear behavior of a single-phase equiatomic TiZrHfNb high-entropy alloy studied using a nanoscratch technique. Acta Mater. 2018;147:78. https://doi.org/10.1016/j.actamat.2018.01.014.

[2] Lu SY, Miao JW, Lu YP. Strengthening and toughening of multi-principal high-entropy alloys. Chin J Rare Met. 2021;45(5):530. https://doi.org/10.13373/j.cnki.cjrm.XY20080042.

[3] Lu Y, Li CY, Tian L, Zhai JS, Kou SZ. Research progress on properties of high-entropy alloys. Chin J Rare Met. 2022;46(10):1352. https://doi.org/10.13373/j.cnki.cjrm.xy19060029.

[4] Verma A, Tarate P, Abhyankar AC, Mohape MR, Gowtam DS, Deshmukh VP, Shanmugasundaram T. High temperature wear in CoCrFeNiCu$_x$ high entropy alloys: the role of Cu. Scripta Mater. 2019;161:28. https://doi.org/10.1016/j.scriptamat.2018.10.007.

[5] Li WD, Xie D, Li DY, Zhang Y, Gao YF, Liaw PK. Mechanical behavior of high-entropy alloys. Prog Mater Sci. 2021;118:100777. https://doi.org/10.1016/j.pmatsci.2021.100777.

[6] Cantor B, Chang ITH, Knight P, Vincent AJB. Microstructural development in equiatomic multicomponent alloys. Mater Sci

Eng A. 2004;375–377:213. https://doi.org/10.1016/j.msea.2003.10.257.

[7] Zhang Y, Zuo TT, Tang Z, Gao MC, Dahmen KA, Liaw PK, Lu ZP. Microstructures and properties of high-entropy alloys. Prog Mater Sci. 2014;61:1. https://doi.org/10.1016/j.pmatsci.2013.10.001.

[8] Gao XF, Chen RR, Liu T, Fang HZ, Qin G, Su YQ, Guo JJ. High-entropy alloys: a review of mechanical properties and deformation mechanisms at cryogenic temperatures. J Mater Sci. 2022;57(12):6573. https://doi.org/10.1007/s10853-022-07066-2.

[9] Wu MY, Chen K, Xu Z, Li DY. Effect of Ti addition on the sliding wear behavior of AlCrFeCoNi high-entropy alloy. Wear. 2020;462–463:203493. https://doi.org/10.1016/j.wear.2020.203493.

[10] Li XF, Feng YH, Liu B, Yi DH, Yang XH, Zhang WD, Chen G, Liu Y, Bai PK. Influence of NbC particles on microstructure and mechanical properties of AlCoCrFeNi high-entropy alloy coatings prepared by laser cladding. J Alloys Compd. 2019;788:485. https://doi.org/10.1016/j.jallcom.2019.02.223.

[11] Ren H, Chen RR, Gao XF, Liu T, Qin G, Wu SP, Guo JJ. Insights on mechanical properties of dual-phase high entropy alloys via Y introduction. J Alloys Compd. 2022;929:167374. https://doi.org/10.1016/j.jallcom.2022.167374.

[12] Zhang LJ, Zhang MD, Zhou Z, Fan JT, Cui P, Yu PF, Jing Q, Ma MZ, Liaw PK, Li G, Liu RP. Effects of rare-earth element, Y, additions on the microstructure and mechanical properties of CoCrFeNi high entropy alloy. Mater Sci Eng A. 2018;725:437. https://doi.org/10.1016/j.msea.2018.04.058.

[13] Lu YP, Gao XX, Dong Y, Wang TM, Chen HL, Mao HH, Zhao YH, Jiang H, Cao ZQ, Li TJ, Guo S. Preparing bulk ultra-fine-microstructure high-entropy alloys via direct solidification. Nanoscale. 2018;10(4):1912. https://doi.org/10.1039/C7NR07281C.

[14] George EP, Raabe D, Ritchie RO. High-entropy alloys. Nat Rev Mater. 2019;4(8):515. https://doi.org/10.1038/s41578-019-0121-4.

[15] Hou JX, Cao BX, Xiao B, Jiao ZB, Yang T. Compositionally complex coherent precipitation-strengthened high-entropy alloys: a critical review. Rare Met. 2022;41(6):2002. https://doi.org/10.1007/s12598-021-01953-4.

[16] Wang H, He QF, Yang Y. High-entropy intermetallics: from alloy design to structural and functional properties. Rare Met. 2022;41(6):1989. https://doi.org/10.1007/s12598-021-01926-7.

[17] Xian X, Zhong ZH, Lin LJ, Zhu ZX, Chen C, Wu YC. Tailoring strength and ductility of high-entropy CrMnFeCoNi alloy by adding Al. Rare Met. 2022;41(3):1015. https://doi.org/10.1007/s12598-018-1161-4.

[18] Wang JJ, Kou ZD, Fu S, Wu SS, Liu SN, Yan MY, Wang D, Lan S, Hahn H, Feng T. Microstructure and magnetic properties evolution of Al/CoCrFeNi nanocrystalline high-entropy alloy composite. Rare Met. 2022;41(6):2038. https://doi.org/10.1007/s12598-021-01931-w.

[19] Zhang WR, Liaw PK, Zhang Y. Science and technology in high-entropy alloys. Sci China Mater. 2018;61(1):2. https://doi.org/10.1007/s40843-017-9195-8.

[20] Ye YF, Wang Q, Lu J, Liu CT, Yang Y. High-entropy alloy: challenges and prospects. Mater Today. 2016;19(6):349. https://doi.org/10.1016/j.mattod.2015.11.026.

[21] Archard JF. Contact and rubbing of flat surfaces. J Appl Phys. 1953;24(8):981. https://doi.org/10.1063/1.1721448.

[22] Luo DW, Zhou Q, Ye WT, Ren Y, Greiner C, He YX, Wang HF. Design and characterization of self-lubricating refractory high entropy alloy-based multilayered films. ACS Appl Mater Inter. 2021;13(46):55712. https://doi.org/10.1021/acsami.1c16949.

[23] Miao JW, Yao HW, Wang J, Lu YP, Wang TM, Li TJ. Surface modification for AlCoCrFeNi$_{2.1}$ eutectic high-entropy alloy via laser remelting technology and subsequent aging heat treatment. J Alloys Compd. 2022;894:162380. https://doi.org/10.1016/j.jallcom.2021.162380.

[24] Geng YS, Chen J, Tan H, Cheng J, Zhu SY, Yang J. Tribological performances of CoCrFeNiAl high entropy alloy matrix solid-lubricating composites over a wide temperature range. Tribol Int. 2021;157:106912. https://doi.org/10.1016/j.triboint.2021.106912.

[25] Miao JW, Liang H, Zhang AJ, He JY, Meng JH, Lu YP. Tribological behavior of an AlCoCrFeNi$_{2.1}$ eutectic high entropy alloy sliding against different counterfaces. Tribol Int. 2021;153:106599. https://doi.org/10.1016/j.triboint.2020.106599.

[26] Jin BQ, Zhang NN, Yu HS, Hao DX, Ma YL. Al$_x$CoCrFeNiSi high entropy alloy coatings with high microhardness and improved wear resistance. Surf Coat Tech. 2020;402:126328. https://doi.org/10.1016/j.surfcoat.2020.126328.

[27] Zhang AJ, Han JS, Su B, Meng JH. A promising new high temperature self-lubricating material: CoCrFeNiS$_{0.5}$ high entropy alloy. Mater Sci Eng A. 2018;731:36. https://doi.org/10.1016/j.msea.2018.06.030.

[28] Li HG, Che PC, Yang XK, Huang YJ, Ning ZL, Sun JF, Fan HB. Enhanced tensile properties and wear resistance of additively manufactured CoCrFeMnNi high-entropy alloy at cryogenic temperature. Rare Met. 2022;41(4):1210. https://doi.org/10.1007/s12598-021-01867-1.

[29] Li ZJ, He JC, Ding XK, Lian GF, Liu M, Chen JF, Dai PQ. Tailoring the surface microstructures and enhancing wear performance of Al$_{0.5}$CoCrFeNiSi$_{0.25}$ high-entropy alloys via laser remelting. Surf Coat Tech. 2023;452:129129. https://doi.org/10.1016/j.surfcoat.2022.129129.

[30] Ren H, Chen RR, Gao XF, Liu T, Qin G, Wu SP, Guo JJ. Development of wear-resistant dual-phase high-entropy alloys enhanced by C15 Laves phase. Mater Charact. 2023;200:112879. https://doi.org/10.1016/j.matchar.2023.112879.

[31] Chuang MH, Tsai MH, Wang WR, Lin SJ, Yeh JW. Microstructure and wear behavior of Al$_x$Co$_{1.5}$CrFeNi$_{1.5}$Ti$_y$ high-entropy alloys. Acta Mater. 2011;59(16):6308. https://doi.org/10.1016/j.actamat.2011.06.041.

[32] Wu JM, Lin SJ, Yeh JW, Chen SK, Huang YS, Chen HC. Adhesive wear behavior of Al$_x$CoCrCuFeNi high-entropy alloys as a function of aluminum content. Wear. 2006;261(5):513. https://doi.org/10.1016/j.wear.2005.12.008.

[33] Chen MR, Lin SJ, Yeh JW, Chuang MH, Chen SK, Huang YS. Effect of vanadium addition on the microstructure, hardness, and wear resistance of Al$_{0.5}$CoCrCuFeNi high-entropy alloy. Metall Mater Trans A. 2006;37(5):1363. https://doi.org/10.1007/s11661-006-0081-3.

[34] An XL, Liu ZD, Zhang LT, Zou Y, Xu XJ, Chu CL, Wei W, Sun WW. A new strong pearlitic multi-principal element alloy to withstand wear at elevated temperatures. Acta Mater. 2022;227:117700. https://doi.org/10.1016/j.actamat.2022.117700.

[35] Jiang H, Jiang L, Qiao DX, Lu YP, Wang TM, Cao ZQ, Li TJ. Effect of niobium on microstructure and properties of the CoCrFeNb$_x$Ni high entropy alloys. J Mater Sci Technol. 2017;33(7):712. https://doi.org/10.1016/j.jmst.2016.09.016.

[36] Jin BQ, Zhang NN, Yin S. Strengthening behavior of AlCoCrFeNi(TiN)$_x$ high-entropy alloy coatings fabricated by plasma spraying and laser remelting. J Mater Sci Technol. 2022;121:163. https://doi.org/10.1016/j.jmst.2021.12.055.

[37] Hsu CY, Yeh JW, Chen SK, Shun TT. Wear resistance and high-temperature compression strength of Fcc CuCoNiCrAl$_{0.5}$Fe alloy with boron addition. Metall Mater Trans A. 2004;35(5):1465. https://doi.org/10.1007/s11661-004-0254-x.

[38] Zhao DC, Kong DC, Huang J, Wang ML, Yamaguchi T, Wang HW. Achieving the lightweight wear-resistant TiC reinforced AlFeCrCo medium-entropy alloy coating on Mg alloy via

resistance seam processing. Scripta Mater. 2022;210:114429. https://doi.org/10.1016/j.scriptamat.2021.114429.

[39] Santodonato LJ, Liaw PK, Unocic RR, Bei H, Morris JR. Predictive multiphase evolution in Al-containing high-entropy alloys. Nat Commun. 2018;9(1):4520. https://doi.org/10.1038/s41467-018-06757-2.

[40] Qin G, Chen RR, Mao HH, Yan Y, Li XJ, Schönecker S, Vitos L, Li XQ. Experimental and theoretical investigations on the phase stability and mechanical properties of $Cr_7Mn_{25}Co_9Ni_{23}Cu_{36}$ high-entropy alloy. Acta Mater. 2021;208:116763. https://doi.org/10.1016/j.actamat.2021.116763.

[41] Chattopadhyay C, Prasad A, Murty BS. Phase prediction in high entropy alloys – a kinetic approach. Acta Mater. 2018;153:214. https://doi.org/10.1016/j.actamat.2018.05.002.

[42] Ren H, Chen RR, Gao XF, Liu T, Qin G, Wu SP, Guo JJ. Phase formation and mechanical features in $(AlCoCrFeNi)_{100-x}Hf_x$ high-entropy alloys: the role of Hf. Mater Sci Eng A. 2022;858:144156. https://doi.org/10.1016/j.msea.2022.144156.

[43] Ren H, Chen RR, Gao XF, Liu T, Qin G, Wu SP, Guo JJ. Sc doping induced the mechanical property improvement of dual-phase high-entropy alloy. Mater Sci Eng A. 2023;862:144425. https://doi.org/10.1016/j.msea.2022.144425.

[44] Ma SG, Zhang Y. Effect of Nb addition on the microstructure and properties of AlCoCrFeNi high-entropy alloy. Mater Sci Eng A. 2012;532:480. https://doi.org/10.1016/j.msea.2011.10.110.

[45] Chen J, Niu PY, Liu YZ, Lu YK, Wang XH, Peng YL, Liu JN. Effect of Zr content on microstructure and mechanical properties of AlCoCrFeNi high entropy alloy. Mater Des. 2016;94:39. https://doi.org/10.1016/j.matdes.2016.01.033.

[46] Winter MJ. WebElements, Periodic Table. University of Sheffield; 1993.

[47] Takeuchi A, Inoue A. Classification of bulk metallic glasses by atomic size difference, heat of mixing and period of constituent elements and its application to characterization of the main alloying element. Mater Trans. 2005;46(12):2817. https://doi.org/10.2320/matertrans.46.2817.

[48] Guo S, Liu CT. Phase stability in high entropy alloys: formation of solid-solution phase or amorphous phase. Prog Nat Sci: Mater Int. 2011;21(6):433. https://doi.org/10.1016/S1002-0071(12)60080-X.

[49] Linden Y, Pinkas M, Munitz A, Meshi L. Long-period antiphase domains and short-range order in a B2 matrix of the AlCoCrFeNi high-entropy alloy. Scripta Mater. 2017;139:49. https://doi.org/10.1016/j.scriptamat.2017.06.015.

[50] Kumar KS, Liu CT. Precipitation in a $Cr–Cr_2Nb$ alloy. Acta Mater. 1997;45(9):3671. https://doi.org/10.1016/S1359-6454(97)00050-5.

[51] Kumar KS, Pang L, Liu CT, Horton J, Kenik EA. Structural stability of the Laves phase Cr_2Ta in a two-phase $Cr–Cr_2Ta$ alloy. Acta Mater. 2000;48(4):911. https://doi.org/10.1016/S1359-6454(99)00377-8.

[52] Huo WY, Zhou H, Fang F, Xie ZH, Jiang JQ. Microstructure and mechanical properties of $CoCrFeNiZr_x$ eutectic high-entropy alloys. Mater Des. 2017;134:226. https://doi.org/10.1016/j.matdes.2017.08.030.

[53] Petch NJ. The cleavage strength of polycrystals. Journal of the Iron and Steel Institute. 1953;174:25. https://doi.org/10.1016/0013-7944(87)90050-6.

[54] Hall EO. The deformation and ageing of mild steel: III discussion of results. Proc Phys Soc Sect B. 1951;64(9):747. https://doi.org/10.1088/0370-1301/64/9/303.

[55] Sriharitha R, Murty BS, Kottada RS. Alloying, thermal stability and strengthening in spark plasma sintered $Al_xCoCrCuFeNi$ high entropy alloys. J Alloys Compd. 2014;583:419. https://doi.org/10.1016/j.jallcom.2013.08.176.

[56] Tabor D. The Hardness of Metals. Oxford: Oxford University Press; 1951.1.

[57] Ma Y, Wang Q, Jiang BB, Li CL, Hao JM, Li XN, Dong C, Nieh TG. Controlled formation of coherent cuboidal nanoprecipitates in body-centered cubic high-entropy alloys based on $Al_2(Ni Co, Fe, Cr)_{14}$ compositions. Acta Mater. 2018;147:213. https://doi.org/10.1016/j.actamat.2018.01.050.

[58] Liu H, Sun SF, Zhang T, Zhang GZ, Yang HF, Hao JB. Effect of Si addition on microstructure and wear behavior of AlCoCrFeNi high-entropy alloy coatings prepared by laser cladding. Surf Coat Tech. 2021;405:126522. https://doi.org/10.1016/j.surfcoat.2020.126522.

[59] Meng JH, Loh NH, Tay BY, Fu G, Tor SB. Tribological behavior of 316L stainless steel fabricated by micro powder injection molding. Wear. 2010;268(7):1013. https://doi.org/10.1016/j.wear.2009.12.033.

[60] Quinn TFJ. Review of oxidational wear: part I: the origins of oxidational wear. Tribol Int. 1983;16(5):257. https://doi.org/10.1016/0301-679X(83)90086-5.

[61] Stott FH. The role of oxidation in the wear of alloys. Tribol Int. 1998;31(1):61. https://doi.org/10.1016/S0301-679X(98)00008-5.

[62] Hasegawa M, Chapter 3.3 - Ellingham Diagram, Edited by S. Seetharaman, Elsevier, Treatise on Process Metallurgy, Boston, 2014;507. Doi: https://doi.org/10.1016/B978-0-08-096986-2.00032-1.